# Multiple Jets of the Antarctic Circumpolar Current South of Australia*

SERGUEI SOKOLOV AND STEPHEN R. RINTOUL

*CSIRO Marine and Atmospheric Research, and Antarctic Climate and Ecosystems Cooperative Research Centre, Hobart, Tasmania, Australia*

(Manuscript received 19 December 2005, in final form 1 December 2006)

ABSTRACT

Maps of the gradient of sea surface height (SSH) and sea surface temperature (SST) reveal that the Antarctic Circumpolar Current (ACC) consists of multiple jets or frontal filaments. The braided and patchy nature of the gradient fields seems at odds with the traditional view, derived from hydrographic sections, that the ACC is made up of three continuous circumpolar fronts. By applying a nonlinear fitting procedure to 638 weekly maps of SSH gradient ($\nabla$SSH), it is shown that the distribution of maxima in $\nabla$SSH (i.e., fronts) is strongly peaked at particular values of absolute SSH (i.e., streamlines). The association between the jets and particular streamlines persists despite strong topographic and eddy–mean flow interactions, which cause the jets to merge, diverge, and fluctuate in intensity along their path. The SSH values corresponding to each frontal branch are nearly constant over the sector of the Southern Ocean between 100°E and 180°. The front positions inferred from SSH agree closely with positions inferred from hydrographic sections using traditional water mass criteria. Recognition of the multiple branches of the Southern Ocean fronts helps to reconcile differences between front locations determined by previous studies. Weekly maps of SSH are used to characterize the structure and variability of the ACC fronts and filaments. The path, width, and intensity of the frontal branches are influenced strongly by the bathymetry. The "meander envelopes" of the fronts are narrow on the northern slope of topographic ridges, where the sloping topography reinforces the $\beta$ effect, and broader over abyssal plains.

## 1. Introduction

For geophysical flows of sufficient spatial scale, the meridional gradient of planetary vorticity (the $\beta$ effect) provides a restoring force that helps to organize the flow into persistent, narrow zonal jets (Rhines 1975). Well-known examples include the jets on Jupiter and the outer planets and the jet streams in the earth's atmosphere. Oceanic flows also fall in a parameter range conducive to the formation of zonal jets, although the presence of land boundaries has been thought to disrupt the generation of continuous jets. The circumpolar channel of the Southern Ocean is an exception to the zonally bounded nature of the ocean basins, and the Antarctic Circumpolar Current (ACC) provides the best oceanic example of the tendency toward zonation of the flow. Zonal jets have recently been found to exist in a number of other ocean basins as well (e.g., Nakano and Hasumi 2005; Maximenko et al. 2005).

The flow of the ACC is well known to be concentrated in several jets associated with fronts, or regions of strong horizontal gradients in water mass properties and sea surface height (Deacon 1937; Nowlin and Clifford 1982; Sievers and Nowlin 1984; Orsi et al. 1995; Belkin and Gordon 1996). It is common, following Orsi et al. (1995), to distinguish three main Southern Ocean fronts, each of them circumpolar in extent and extending from the sea surface to the deep ocean: from north to south, these fronts are the subantarctic front (SAF), the polar front (PF), and the southern ACC front (sACCf). A fourth feature, the southern boundary of the ACC (Bdy), marks the southern limit of the current. The fact that the fronts coincide with particular water mass features means that simple phenomenologi-

* This paper is an addition to the collection of papers published in the February 2007 *Journal of Physical Oceanography* Special Issue in Honor of Carl Wunsch (see acknowledgments).

*Corresponding author address:* Serguei Sokolov, CSIRO Marine and Atmospheric Research, and Antarctic Climate and Ecosystems Cooperative Research Centre, Hobart, TAS 7001, Australia.
E-mail: serguei.sokolov@csiro.au

DOI: 10.1175/JPO3111.1

cal criteria such as the location of a particular isotherm at a particular depth can be used to locate the fronts (e.g., the PF is often associated with the northern limit of the temperature minimum layer near 200 m). Perhaps surprisingly, the same simple criteria can be used to locate the fronts along much or all of their circumpolar extent, indicating the persistence of the fronts. Useful summaries of the various criteria used to define Southern Ocean fronts can be found in Peterson and Stramma (1991), Orsi et al. (1995), and Belkin and Gordon (1996).

However, while the fronts are robust features of the Southern Ocean, recent high-resolution observations from ships and satellites have made it clear that the frontal structure of the ACC is more complex than previously inferred from measurements with coarser sampling (e.g., Hughes and Ash 2001). Many of the major ACC fronts consist of multiple branches or filaments, which merge and diverge along the circumpolar path. An example is shown in Fig. 1. Because the ACC fronts are associated with large geostrophic currents, the fronts are clearly seen in maps of the gradient of sea surface height ($\nabla$SSH). The distribution of $\nabla$SSH versus latitude and time at 130°E shows the multiple filaments of the ACC, with between six and nine maxima observed at any one time. While the structure is complex—jets merge and split, and weaken and strengthen—there is also substantial persistence in both space and time: $\nabla$SSH maxima tend to recur at similar latitudes and to be maintained for many months. Multiple branches are evident even in multiyear averages of sea surface temperature gradients (Hughes and Ash 2001) and of surface velocity derived from drifter data (Niiler et al. 2003). High-resolution numerical models also suggest that the ACC has a much more complex frontal structure than is evident in maps based on sparse historical hydrographic data (e.g., Maltrud et al. 1998; Best et al. 1999; Hughes and Ash 2001).

Here we reconsider the nature of the frontal structure of the Southern Ocean, to see if these two disparate views can be reconciled. How is it that hydrographic data suggest that the ACC consists of three fronts associated with particular temperature or salinity features along their complete circumpolar path, while high-resolution models and satellite observations show that the ACC consists of a larger number of discontinuous filaments? While the ACC has often been suggested to provide an oceanic example of the tendency to develop zonal jets, no connection has yet been made between the multiple jets present in high-resolution simulations of large-scale turbulent flows and the ACC fronts described by hydrographers.

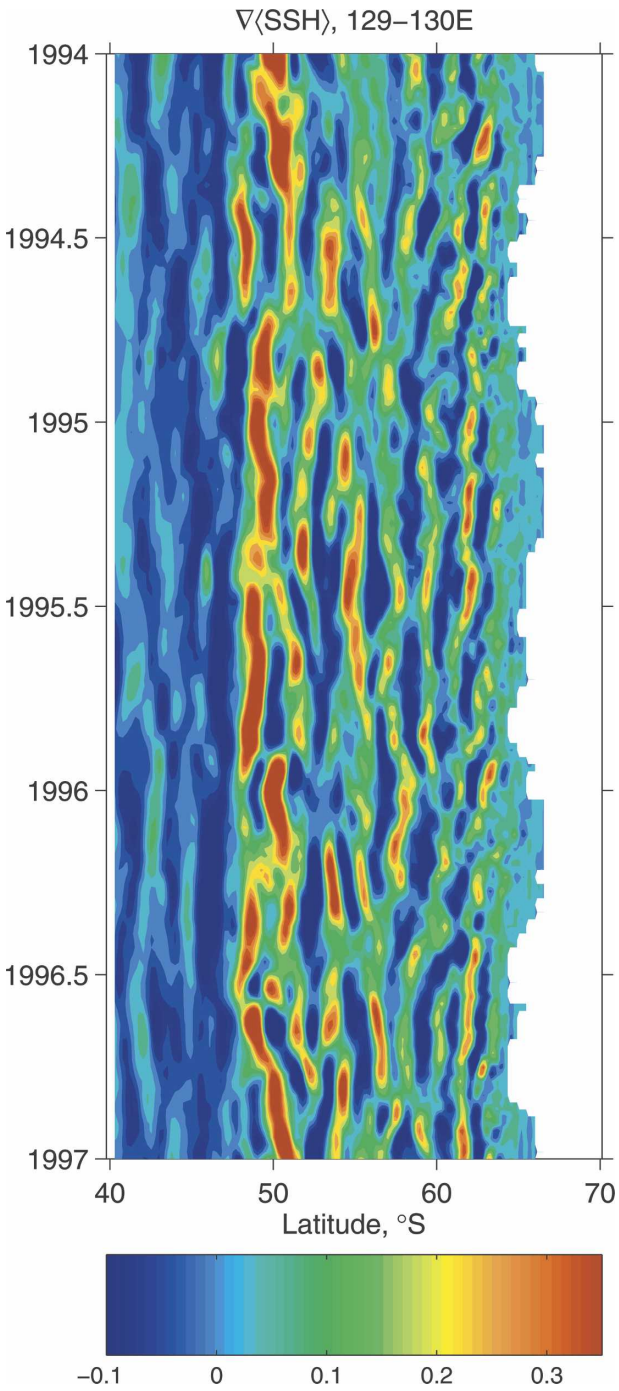


FIG. 1. Meridional gradient of sea surface height [m (100 km)$^{-1}$] at 130°E between 1994 and 1997.

## 2. Background: Dynamic and kinematic views of the ACC jets

### *a. Dynamical perspective on the jets of the ACC*

Jets—"localized, elongated, energetic flows, usually with persistence in time" (Rhines 1994)—are common

features of large-scale planetary flows. The $\beta$ effect facilitates the self-organization of barotropic two-dimensional turbulence into elongated zonal flows (Rhines 1975). The meridional scale of the jets is given by $k = (\beta/2U)^{1/2}$, where $k$ is the meridional wavenumber, $\beta$ is the variation of the Coriolis parameter with latitude, and $U$ is a characteristic eddy velocity. Once established, the jets often persist for long periods, maintained by eddy–mean flow interactions. The tendency to form jets is common to both barotropic and baroclinic flows. In the baroclinic case, baroclinic instability causes growth at the scale of the Rossby radius of deformation, followed by a tendency for the eddies to become more barotropic and to establish zonal jets (Rhines 1977; Panetta 1993; McWilliams et al. 1978). The baroclinic jets are much stronger than in the barotropic case, fueled by release of potential energy in the mean baroclinic flow. If the domain is sufficiently wide (relative to the Rossby radius), multiple, persistent jets are formed (Panetta 1993).

Topography can influence the formation of jets in a number of ways. Topography sloping in the meridional direction provides an analog to the $\beta$-effect, augmenting or reducing the restoring force of the planetary vorticity gradient (e.g., Sinha and Richards 1999). The presence of topography allows correlations between streamfunction and depth to be established, creating the bottom form stress that is now known to balance the wind forcing of the ACC (Munk and Palmén 1951; Rintoul et al. 2001; Olbers et al. 2004). Channel models of the ACC including topography produce one or more narrow jets when driven by wind forcing with large meridional scale (e.g., Wolff et al. 1991; Treguier and McWilliams 1990; Treguier and Panetta 1994; Sinha and Richards 1999). Jets can also form as a result of blocking and steering of the flow by isolated topography (Rhines 1989; Tansley and Marshall 2001). Full primitive-equation models with realistic bathymetry produce a complex web of many jets, which merge and diverge along the circumpolar path of the ACC [e.g., Sinha and Richards (1999) find between 6 and 10 jets in the Fine-Resolution Antarctic Model (FRAM) and Parallel Ocean Program (POP) models].

### b. Hydrographic view of the ACC jets

There are therefore strong dynamical reasons to expect the flow of the ACC to be organized into a number of narrow jets. However, the connection between the apparently discontinuous jets produced in high-resolution numerical simulations and the circumpolar fronts identified in hydrographic data is not clear. Deacon (1937) first noted that density surfaces shoaled to the south across the ACC in a series of sharp steps, rather than as a smooth ramp. Orsi et al. (1995) and Belkin and Gordon (1996) used hydrographic sections to demonstrate that the ACC consists of three circumpolar fronts (the subantarctic front, the polar front, and the southern ACC front) that could be reliably identified at any longitude using a set of simple criteria based on water mass properties. For example, the subantarctic front has been identified by the presence of a thermostad (the Subantarctic Mode Water) to the north; the presence of a well-defined salinity minimum (the Antarctic Intermediate Water) to the north; and the location of the 4°–5°C isotherm at 400-m depth, among other criteria.

While there is widespread agreement that the ACC consists of several continuous, circumpolar fronts, some debate remains over the number and location of the fronts. The use of slightly different criteria by different authors has created some confusion in the literature. For example, while the Orsi et al. (1995) and Belkin and Gordon (1996) front positions broadly agree, in some locations the position of the SAF differs by more than 500 km in the two studies, both of which are based on essentially the same hydrographic data. Other studies have suggested that the primary fronts sometimes split into two or more branches (e.g., Sievers and Nowlin 1984; Sparrow et al. 1996; Moore et al. 1999; Rintoul and Bullister 1999). Pollard et al. (2002) noted several current jets in the southwest Indian Ocean and concluded that the fronts of the ACC were not circumpolar after all.

### c. A view of the ACC jets from remote sensing

Several studies have used observations from satellites to locate ACC fronts. The global coverage and relatively rapid repeat cycle of satellite observations allows maps of the ACC to be constructed with much greater detail than is possible from hydrographic data. For example, Gille (1994) mapped the SAF and PF by fitting two meandering Gaussian jets to the SSH field. Her maps show the two fronts running parallel and close to each other along the circumpolar path of the ACC. In a number of regions, the front locations differ markedly from those inferred from hydrography; in particular, her PF lies farther north than found in the maps of Orsi et al. and Belkin and Gordon. Hughes and Ash (2001) used satellite measurements of sea surface temperature (SST) to identify ACC fronts, by equating fronts with regions of enhanced SST gradient. Their maps of mean $\nabla$SST show multiple narrow filaments that merge and diverge along the circumpolar path, but which are remarkably stable in space (the mean is calculated over

44 months). Hughes and Ash were unable to say how the SST fronts corresponded to the fronts identified in hydrographic data and concluded in any case that there was little evidence of circumpolar fronts.

In summary, theory and numerical simulations, hydrographic data, and remote sensing produce disparate views of the ACC jets. One goal of this paper is to reconcile these differing perspectives. Sokolov and Rintoul (2002, hereinafter SR02) took a first step in this direction by examining repeat, high-resolution hydrographic sections near 140°E. At this meridian, they found that each of the major fronts was consistently split into two or more branches. Each of the branches coincided with water mass features similar to those traditionally used to define the major ACC fronts (e.g., Orsi et al. 1995; Belkin and Gordon 1996) and so could be unambiguously identified as a branch of the SAF, the PF, or the sACCf. These branches were located as much as 500 km apart in some cases; at other times, filaments were found to have coalesced into a single strong feature. SR02 concluded that, at least at this location, hydrographic sections with sufficient spatial resolution reveal a filamented structure to the ACC more akin to that seen in satellite data and models than the classical three-front picture of the current. They further showed that each of the frontal branches observed at 140°E coincided with a transport maximum or jet. Finally, SR02 showed that each frontal branch at 140°E coincided with a relatively narrow range of SSH values (or streamlines). This observation suggested to them that the fronts might be mapped using SSH, but with their data they could not test whether the association between each frontal branch and a particular streamline was a local phenomenon or held more widely.

Here we test the hypothesis that the fronts of the ACC coincide with streamlines defined by SSH by examining a wider region south of Australia and New Zealand (100°E–180°). We examine the distribution of maxima in the gradient of SSH (i.e., jets) in streamfunction–space and find that the distribution is sharply peaked at particular values of the streamfunction. The SSH values corresponding to the gradient maxima are very similar to those found to be associated with particular ACC fronts identified in hydrographic data at 140°E, allowing us to associate each streamline with a particular front.

## 3. Data and methods

We use 12 yr of weekly SSH maps to identify fronts south of Australia and New Zealand in the region between 100°E and 180°. Specifically, we used the Collecte, Localisation, Satellites (CLS)/Archiving, Validation, and Interpretation of Satellite Oceanographic Data (AVISO) "Mean Sea Level Anomaly" (MSLA) maps, which are produced by mapping data from the Ocean Topography Experiment (TOPEX)/Poseidon (T/P), *European Remote-Sensing Satellites 1 and 2* (*ERS-1* and *ERS-2*) altimeters (Le Traon et al. 1998). The combination of T/P and ERS data enables signals with wavelengths longer than 100 km to be recovered in our region of interest; wavelengths of 50 km are present but reduced in energy by about 50% (Morrow et al. 2003). Wind forcing drives high-frequency (periods of a few days) energetic barotropic motions with large spatial scales [$O$(1000 km)] in some parts of the Southern Ocean (e.g., Webb and de Cuevas 2003), providing a potential source of aliasing in altimeter data (Stammer et al. 2000). The removal of long wavelength errors by the mapping method tends to minimize the aliasing of high-frequency variability with large spatial scale, but some aliasing of motions with periods less than 20 days and wavelengths less than 500 km will remain in the dataset (Ducet et al. 2000). The mean mapping error of the SSH fields is less than 10% of the signal variance (or $<2$ cm in our region); for comparison, the change in SSH across the major Southern Ocean fronts varies from about 20 to 60 cm. To produce maps of absolute SSH, we added the anomalies to the mean surface dynamic height (relative to 2500 dbar) derived from the Olbers et al. (1992) climatology, as in SR02. We use a reference level of 2500 m for the mean dynamic height field to capture most of the signal of the deep-reaching ACC fronts, while remaining sufficiently shallow to be defined in most of the Southern Ocean. Using this approach, we cannot track the fronts in waters shallower than 2500 m. The conclusion that fronts coincide with particular streamlines is insensitive to the choice of mean field, as shown in the appendix.

We subdivided the region south of Australia and New Zealand (Fig. 2) into three sectors (100°–130°E, 130°–160°E, and 160°E–180°) and used the 12-yr sequence of weekly SSH maps to test the hypothesis that particular SSH contours tend to coincide with zones of large SSH gradients (fronts). All high gradient zones, including those associated with eddies, were included in the optimization. A threshold of 0.25 m $(100\ \text{km})^{-1}$ was used to define the high $\nabla$SSH regions. This value was chosen to include the weaker southern fronts (e.g., sACCf and Bdy) and corresponds to the 85th percentile of the empirical distribution of the SSH gradients in the region. Note that the $\nabla$SSH field is dominated by the gradients associated with the SSH anomaly field, with gradients of the SSH climatology typically smaller by a factor of 3 (see the appendix for further discussion).

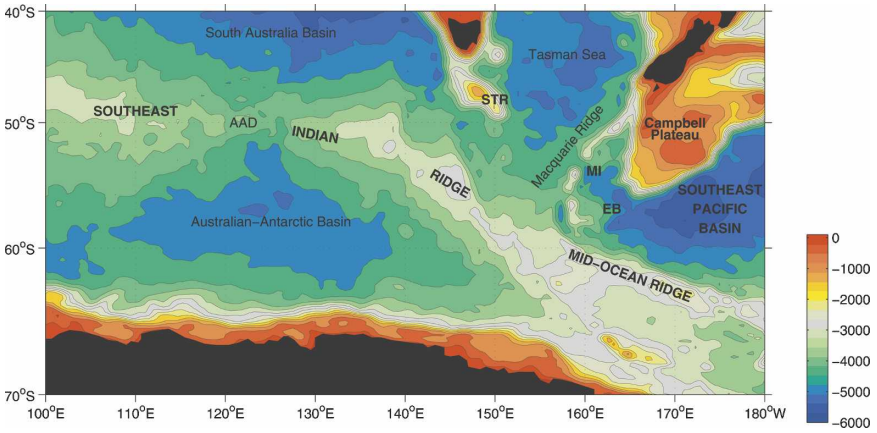


FIG. 2. Bathymetry of the study region south of Australia and New Zealand. (STR = South Tasman Rise; MI = Macquarie Island; EB = Emerald Basin; AAD = Australian–Antarctic Discordance).

The unknown SSH contours $\zeta_i$ associated with fronts were obtained by minimizing the functional $\Re$ defined as

$$\Re(\zeta) = 1 - \sum_{i=1:n} S_{\zeta_i} \Big/ S,$$

where $S$ is the total area where $\nabla\zeta > 0.25$ m $(100\ \text{km})^{-1}$, $S_{\zeta_i}$ is the area [with $\nabla\zeta > 0.25$ m $(100\ \text{km})^{-1}$] covered by contour $\zeta_i$ with width given in Fig. 3a, and $n$ is the number of frontal branches. As the minimization problem is a function of area, we need to associate a width with each frontal branch. We define the width as the distance over which $\nabla$SSH exceeds the threshold value. The width of each front was estimated only in areas where enhanced SSH gradients were associated with a single front. Defined in this way, the mean width of the Southern Ocean fronts decreases from 1° of latitude for the branches of the SAF in the north to values of less than 0.5° of latitude for the southern fronts, although variability in the width of the fronts is large, as reflected in the error bars in Fig. 3a. The decrease in width of the fronts with increasing latitude is visible in maps of $\nabla$SSH (e.g., Fig. 1) and expected given the inverse dependence on $f$ of the baroclinic Rossby radius of deformation. We anticipate that the location of the fronts will be insensitive to the width assumed, while the fraction of the total SSH variance accounted for by a given number of contours $n$ will depend somewhat on the width (assumption of a narrower width will mean each contour occupies less area and explains less variance).

Figures 3b and 3c illustrate how well the distribution of $\nabla$SSH maxima can be explained as the number of contours in the fit increases. The single contour that accounts for the largest area of $\nabla$SSH maxima is at $\zeta_i$ = 1.8 m (Fig. 3c) and results in a 30%–50% reduction in $\Re$ (depending on which longitude sector is considered; Fig. 3b). Comparison to the SR02 results at 140°E suggests that this contour corresponds to the SAF. Three contours is sufficient to reduce $\Re$ by 55%–75%, and the SSH values in this case correspond to two branches of the SAF and a third branch, which is a "compromise" between SSH values found to coincide with the northern branch of the PF and the southern branch of the SAF by SR02 at 140°E. As the number of SSH contours is increased further, the northern and middle branches of the SAF remain at similar values of SSH and contours corresponding to additional frontal branches are introduced. Ten SSH contours are sufficient to account for 92% of all $\nabla$SSH values above the threshold. While the southern fronts (sACCf and Bdy) make the smallest contribution to the decrease in $\Re$, the distribution of maxima in $\nabla$SSH nevertheless shows clear peaks in the range of SSH corresponding to the southern fronts, as shown below. The optimization gives results similar to those of SR02, with regard to both the number of fronts and the value of SSH corresponding to each front.

The best-fit or optimal contours $\zeta_i$ do a good job of explaining the distribution of enhanced gradients in the SSH fields (Fig. 3d), particularly in the range of SSH values corresponding to the SAF and PF. The southern- and northernmost features (Bdy and SAZ) coincide with less than 70% of the high SSH gradients in their SSH range. SSH gradients in both regions are relatively weak. In addition, the Bdy front is close to the Antarctic continental margin where the SSH satellite observations are most affected by sea ice cover. The weak gradient extrema in the SAZ do not correspond to either the SAF or the subtropical front (STF) and are not as well described by a single SSH value, as discussed below.

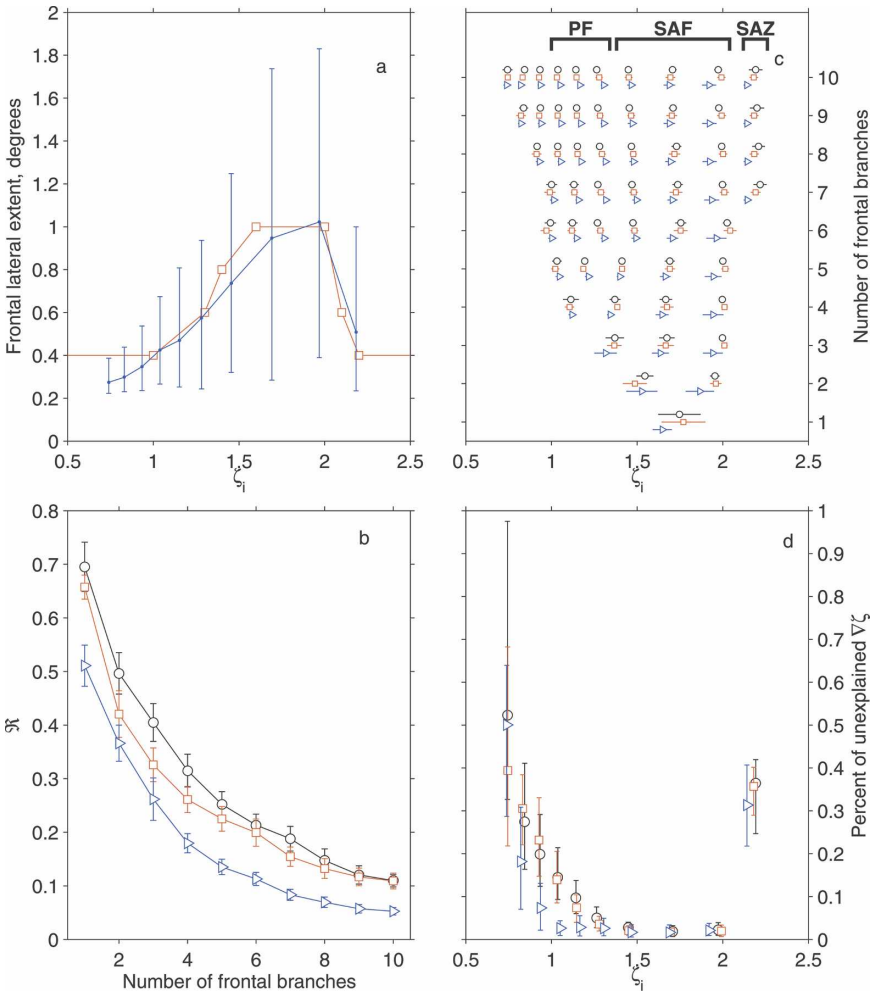


FIG. 3. Fitting SSH contours to the ∇SSH field. (a) Width of each frontal branch, defined as the distance over which ∇SSH $> 0.25$ m (100 km)$^{-1}$. Dots with error bars are estimates from SSH maps; squares show the approximation used in this study. Error bars are represented by 10th and 90th percentiles of the front width distributions. (b) Mean reduction in $\Re$ as the number of frontal branches used in the optimization is increased. Three lines with symbols represent three subregions: circles (western), squares (central), and triangles (eastern). Standard deviations of estimates are shown by error bars. (c) Optimal or best-fit SSH contours $\zeta_i$ as the number of frontal branches used in the optimization is increased. Symbols are as in (b). Standard deviations of optimal $\zeta_i$ are indicated by horizontal lines. (d) Fraction of the enhanced SSH gradient (sampled in each $\zeta_i$ SSH range) that is unexplained by optimal contours $\zeta_i$. Symbols are as in (b). Error bars are represented by 10th and 90th percentiles of error distributions.

## 4. Results

### a. *Distribution of ACC fronts in streamfunction space*

Figure 4 shows histograms of the 10 "best-fit" SSH contours for each of the three sectors derived from the weekly maps of SSH. Each of the histograms has a sharply defined peak, centered on a modal or "core" streamline corresponding to each frontal branch. The histograms for each branch are clearly distinct and do not overlap (except for the southernmost fronts, which are closely spaced in SSH). Standard deviations of the best-fit SSH contour values relative to the mean SSH value for each front do not exceed 3 cm, 5 to 10 times smaller than the difference in SSH between adjacent fronts (Table 1; the column labeled SAZ is a special case, discussed below). Each filament is separated from adjacent filaments by bands of weaker flow, corre-

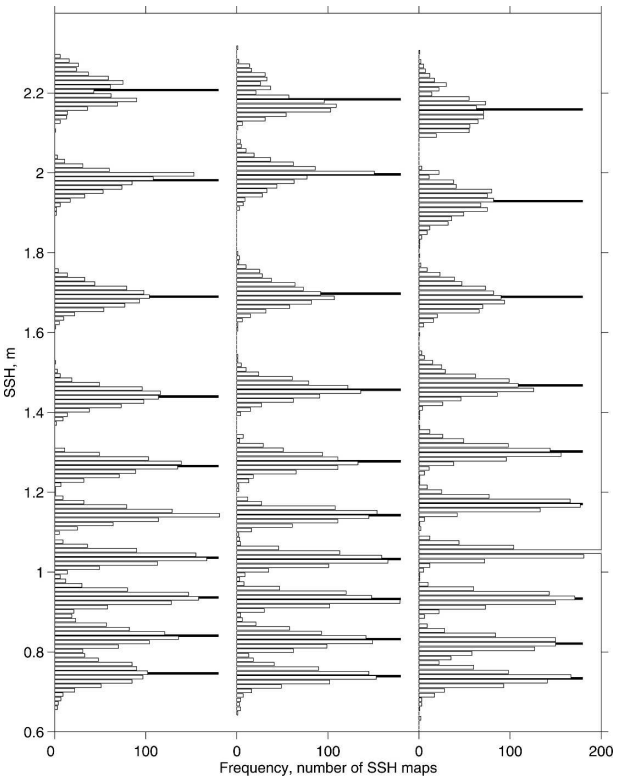


FIG. 4. Frequency distribution of optimized SSH contours obtained for frontal branches in three sectors of the Southern Ocean: (left) sector 100°–130°E; (middle) sector 130°–160°E; and (right) sector 160°E–180°. Frequency is the number of SSH maps for which that value of SSH coincided with a maximum in $\nabla$SSH. A total of 638 SSH maps were used. Mean SSH values for each frontal branch are indicated by solid horizontal lines.

sponding to a range of streamlines along which enhanced gradients of SSH are rarely present. Furthermore, the deviations from the mean value for each branch are dominated by periods less than 4 months (Table 1); the standard deviations of the SSH contours at longer time scales are all less than 1 cm. The modal SSH values associated with each front change by only 2–3 cm across the region between 100°E and 180°. We conclude from Fig. 4 that there is close alignment between the ACC fronts and particular streamlines throughout a sector spanning nearly one-quarter of the circumpolar path of the current.

A typical synoptic $\nabla$SSH field is shown in Fig. 5, overlaid with the best-fit SSH contours. The map shows a large number of discontinuous filaments of elevated $\nabla$SSH. In the absence of any additional information, it is difficult to determine the connection, if any, between different maxima in the gradient field. The contours show that the best-fit SSH contours derived from the 12-yr sequence of weekly maps (i.e., not the fit to this particular synoptic map) pass through essentially all the regions where the gradient exceeds the threshold value. While the patchy distribution of $\nabla$SSH maxima suggests little in the way of continuous fronts, the fact that the optimized SSH contours do a good job of tracking the high $\nabla$SSH regions indicates that the frontal structure of the ACC is persistent and robust. Individual frontal branches merge and diverge as they traverse the region, intensifying or weakening the gradient of SSH, but each filament remains "locked" to a particular streamline.

The results of the optimization procedure suggest that the multiple branches or filaments found at 140°E by SR02 are found throughout the 100°E to 180° sector. In addition, the optimization suggests that a third distinct branch of the Polar Front exists over the South Indian Basin at 115°–125°E, the Southeast Indian Ridge at 135°–145°E, and the Macquarie Ridge and Emerald Basin at 155°–165°E (Figs. 3 and 5); elsewhere it is merged with either the northern or southern branch of the PF.

TABLE 1. Optimized SSH values (m) associated with the frontal branches in three sectors of the Southern Ocean based on the 12-yr dataset of weekly SSH maps. (N, M, and S denote the northern, middle, and southern branches, respectively.) "Total std dev" is the standard deviation about the mean value, including variability at all periods. "Mesoscale std dev" is the standard deviation of variability with periods less than 4 months.

| | Sector 100°–130°E | | | Sector 130°–160°E | | | Sector 160°E–180° | | | 100°E–180° region |
|---|---|---|---|---|---|---|---|---|---|---|
| Fronts | Mean | Total std dev | Mesoscale std dev | Mean | Total std dev | Mesoscale std dev | Mean | Total std dev | Mesoscale std dev | Mean |
| SAZ | 2.21 | 0.036 | 0.022 | 2.18 | 0.035 | 0.018 | 2.16 | 0.040 | 0.024 | 2.18 |
| SAF-N | 1.98 | 0.024 | 0.019 | 2.00 | 0.029 | 0.020 | 1.93 | 0.035 | 0.026 | 1.97 |
| SAF-M | 1.69 | 0.026 | 0.020 | 1.70 | 0.030 | 0.023 | 1.69 | 0.030 | 0.024 | 1.69 |
| SAF-S | 1.44 | 0.023 | 0.019 | 1.46 | 0.023 | 0.016 | 1.47 | 0.026 | 0.020 | 1.45 |
| PF-N | 1.27 | 0.019 | 0.016 | 1.28 | 0.022 | 0.014 | 1.30 | 0.020 | 0.016 | 1.28 |
| PF-M | 1.14 | 0.017 | 0.014 | 1.14 | 0.017 | 0.013 | 1.17 | 0.015 | 0.013 | 1.15 |
| PF-S | 1.04 | 0.016 | 0.013 | 1.03 | 0.015 | 0.012 | 1.05 | 0.014 | 0.012 | 1.04 |
| sACCf-N | 0.94 | 0.017 | 0.014 | 0.93 | 0.015 | 0.012 | 0.93 | 0.016 | 0.013 | 0.93 |
| sACCf-S | 0.84 | 0.021 | 0.016 | 0.83 | 0.018 | 0.015 | 0.82 | 0.017 | 0.014 | 0.83 |
| Bdy | 0.75 | 0.026 | 0.020 | 0.74 | 0.020 | 0.017 | 0.73 | 0.021 | 0.016 | 0.74 |

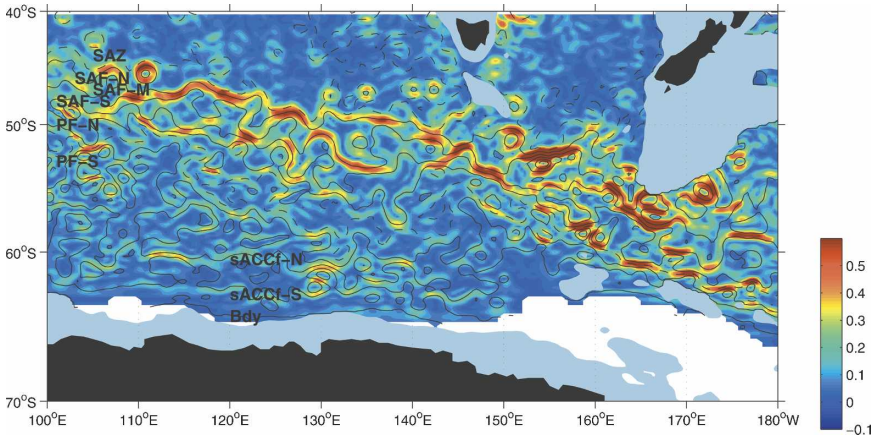


FIG. 5. A typical SSH gradient field south of Australia and New Zealand (3 Jul 2002) overlaid with the mean best-fit SSH contours optimized for the whole period of observations (given in the last column of Table 1). The contours corresponding to the SAZ feature and the middle branch of the PF are dashed, for clarity. Depths shallower than 2500 m are shaded.

### b. *Mean (climatological) frontal structure in the region*

The gradient of the mean SSH field is shown in Fig. 6, overlaid with the mean position of the best-fit SSH contours corresponding to each frontal branch (Table 1). There is substantial structure in the field, despite being the gradient of the 12-yr mean. The strongest gradients tend to be found in the northern Southern Ocean, along the SAF, in particular where filaments merge to form a single strong front. The PF corresponds to a strong maximum near 60°S, 170°E. Moderate gradients are found over the abyssal plain of the Australian–Antarctic Basin, corresponding to branches of the PF, the sACCf, and the Bdy. The SAZ is characterized by very weak gradients.

Shifts in the latitude or orientation of the fronts are influenced strongly by the bathymetry (cf. Fig. 6 to Fig. 2). The bathymetry is sufficiently large to cause significant deviations of the planetary vorticity contours from lines of constant latitude. Perturbations in the path of the fronts as water columns attempt to conserve their planetary vorticity often cause frontal branches to merge or diverge. For example, all three branches of the SAF and the northern branch of the PF often merge south of Tasmania, producing a strong maximum in $\nabla$SSH. This feature coincides with the shoaling and change in orientation of the Southeast Indian Ridge (SEIR). The SAF branches tend to merge southwest of the Campbell Plateau where the fronts are forced to pass to the south of the plateau. Just up- and downstream of this feature, the branches tend to diverge over

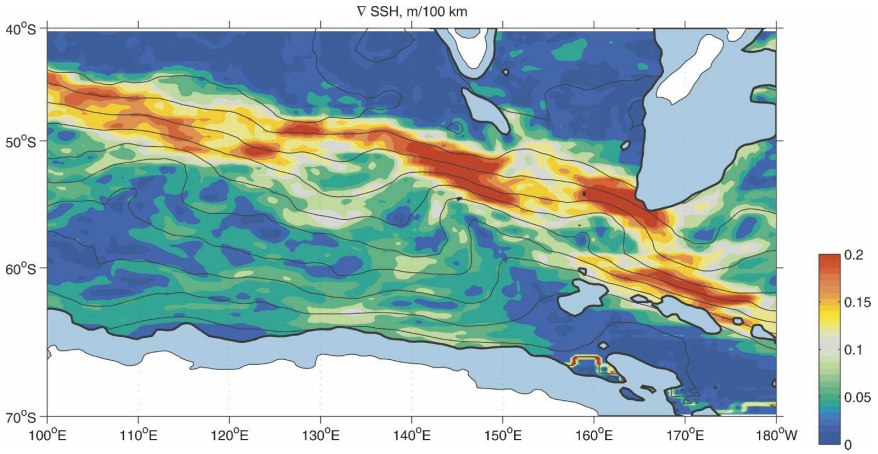


FIG. 6. Gradient of mean SSH [m (100 km)$^{-1}$] overlaid with the mean position of the Southern Ocean fronts. Depths shallower than 2500 m are shaded.

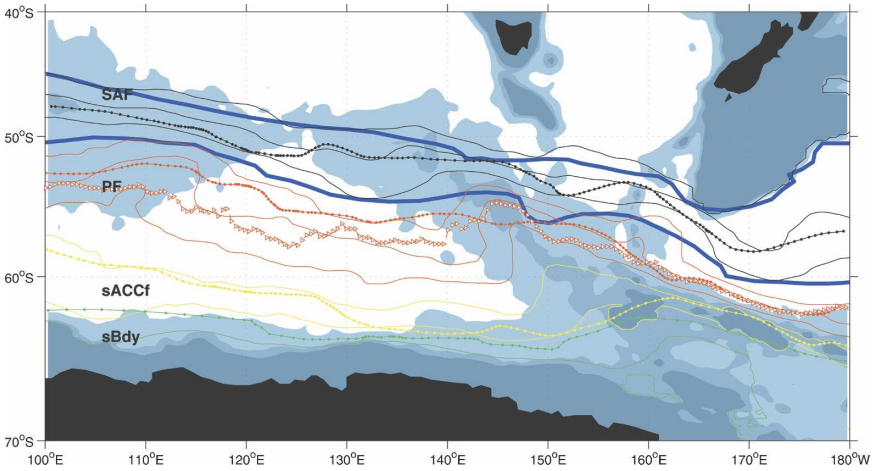


FIG. 7. Comparison between Southern Ocean front positions mapped using SSH (m) and positions reported by Belkin and Gordon (1996; thick blue line), Orsi et al. (1995; solid lines with solid symbols), and Moore et al. (1999; solid lines with open triangles). The Southern Ocean fronts (except Belkin and Gordon) are color coded: SAF is black, PF is red, sACCf is yellow, Bdy is green, and SAZ/STF is blue. The bathymetry is shaded (the 4000-, 3000-, and 2500-m contours are shown).

the deep abyssal plain. The northern branch of the SAF follows the edge of the Campbell Plateau, while the middle and southern branches turn sharply to the south east of 165°E. Similarly, the branches of the PF and sACCf merge to form a single frontal zone on the northern flank of the SEIR near 170°E. Over deep oceanic basins the ACC frontal branches are well separated. For example, the frontal branches of the PF, the sACCf, and the Bdy are clearly distinct over the deep Australian–Antarctic Basin.

### c. *Comparison of front positions derived from SSH to results of previous studies*

The various hydrographic criteria used in previous studies have caused some confusion in the literature, with different studies placing the same feature hundreds of kilometers apart. For example, the Belkin and Gordon (1996) position of the SAF is always north of that of Orsi et al. (1995) in this sector, sometimes by as much as 500 km (e.g., south of the Campbell Plateau). An appreciation of the multiple branches of the Southern Ocean fronts helps to explain many of these discrepancies.

For example, SR02 found three branches of the SAF corresponding to maxima in horizontal gradients of temperature, salinity, and density. The northern SAF corresponded to a decrease in potential temperature ($\theta$) from $>8°$ to $<6°$C at 300 to 400 dbar, the middle branch from $>6°$ to $<5°$C; and the southern SAF coincided with a decrease in $\theta$ from $>5°$ to $<3°$C at the same depths. Belkin and Gordon (1996) used the presence of the low salinity tongue of Antarctic Intermediate Water and the thermostad of Subantarctic Mode Water just to the north to identify the SAF in this sector, placing the SAF at a temperature of 6°C at 400-m depth. This criterion is similar to the definition of the northern branch of the SAF in SR02. Orsi et al. (1995) used a criterion of 4°–5°C at 400-m depth, which is similar to the SR02 definition of the middle or southern branch of the SAF. Figure 7 illustrates that in fact the Belkin and Gordon SAF closely follows the northern branch identified here, while the Orsi et al. SAF oscillates between the middle and southern branch.

Previous studies also disagree over the position of the PF. SR02 find that the northern and southern branches of the PF correspond to the northern limit of 2°C water in the temperature minimum and the southern limit of water warmer than 2.2°C in the temperature maximum layer, respectively. At 140°E, these features are typically separated by 500 km or more. Belkin and Gordon (1996) used the northernmost extent of the subsurface temperature minimum cooler than 2°C, which corresponds to the northern branch of the PF. Orsi et al. (1995) used both of the above criteria to map the PF, leading to ambiguity in those sectors where the features were not coincident. Moore et al. (1999) found that in some regions of the Southern Ocean (west of Drake Passage and in the southwestern Pacific in particular) two distinct zones of enhanced surface temperature gradients are observed in the temperature range of the PF. In these regions they used the more poleward front. Therefore the position of the PF derived by Moore et

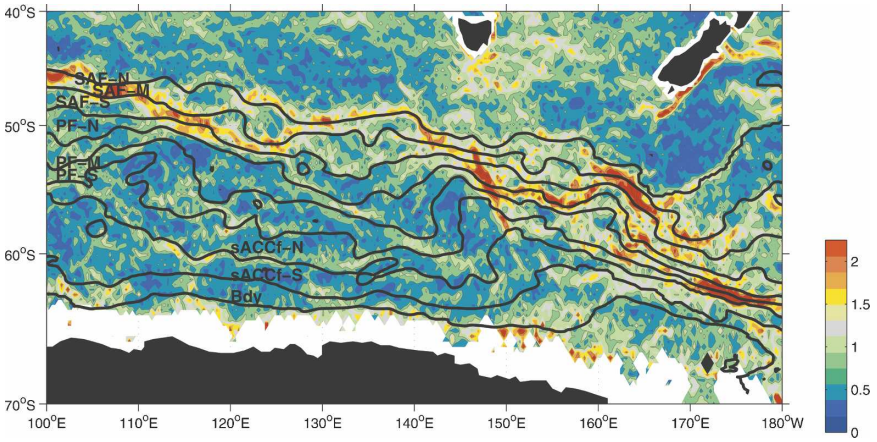


FIG. 8. Annual average front positions for 1993 overlaid on the annual mean sea surface temperature gradient [°C (100 km)$^{-1}$]. SST data are from the National Oceanic and Atmospheric Administration–National Aeronautics and Space Administration (NOAA–NASA) Pathfinder reanalysis of Advanced Very High Resolution Radiometer data.

al. (1999) might be expected to correspond to the southern branch of the PF. The existence of multiple branches of the PF can explain the systematic offsets between the three earlier studies: the Belkin and Gordon PF lies close to the northern branch; the Orsi et al. PF lies consistently to the south of the Belkin and Gordon position and corresponds to either the northern or middle branch; and the Moore et al. PF is found even farther south, between the middle and southern branches. The front positions derived from $\nabla$SSH suggest that the different criteria used by previous authors selected different branches of the primary fronts.

The front positions derived from historical hydrographic data are also smoother than those derived from SSH. For example, the Orsi et al. and Belkin and Gordon maps miss the sharp northward deflection of the PF branches as they encounter the SEIR between 140° and 150°E. This feature does, however, appear in the PF path derived from high-resolution SST data by Moore et al.

Gille (1994) used SSH to locate Southern Ocean fronts. She fit two Gaussian jets to the SSH field, on the assumption that the ACC consisted of two major fronts. The many filaments present in maps of $\nabla$SSH and $\nabla$SST (e.g., Fig. 1; Hughes and Ash 2001) suggest that the two-jet approximation is not very appropriate for the ACC. In the Australian–New Zealand sector, Fig. 3c suggests that a two-jet model would tend to pick out two branches of the SAF, rather than the SAF and PF (i.e., the two branches of the SAF make the largest contribution to the total variance). Indeed, in her study the PF closely follows the SAF and is offset well to the north of the PF position inferred from hydrographic data (e.g., Gordon 1972; Orsi et al. 1995; Belkin and Gordon 1996; SR02; Budillon and Rintoul 2003).

SST has also been used to identify Southern Ocean fronts (e.g., Moore et al. 1999). SST may be affected by air–sea exchange (e.g., heating, wind mixing, or Ekman transport), which may mask or displace the surface signature of a deep front. Frequent cloud cover over the Southern Ocean also reduces the effectiveness with which the ACC fronts can be tracked using satellite observations of SST. Nevertheless, Fig. 8 suggests that there is generally good correspondence between the frontal branches inferred from SSH and the $\nabla$SST field, even when averaged over a year. The largest SST gradients can be explained by the merging of several frontal branches (e.g., along the SAF near 115°E and southwest of the Campbell Plateau, or along the PF and sACCf east of 170°E). Where they are separated, the branches of the SAF tend to correspond to distinct maxima in $\nabla$SST. Note that the northern branch of the SAF is clearly defined in $\nabla$SST as it follows the southern edge of the Campbell Plateau and corresponds closely to the position of this branch inferred from SSH. The enhanced gradients of SST in the SAZ and immediately south of New Zealand reflect the STF and associated eddies; while the STF has a clear signature in $\nabla$SST, the temperature and salinity changes across the STF are almost density-compensating (e.g., SR02) and so there is little signature of this front in SSH. The southern fronts are also not very evident in $\nabla$SST. In this region the SST changes are small and there are larger gaps in the SST dataset due to the presence of clouds and sea ice. Overall, there is good consistency between fronts inferred from gradients of SSH and of

SST. The front locations inferred from SSH aid in the interpretation of the patchy ∇SST field.

### *d. SSH gradients in the SAZ*

Enhanced gradients in the SAZ tend to coincide with an SSH value of about 2.18 m. This feature is surprising, as there are no deep-reaching fronts in the SAZ like those found in the ACC and the water mass structure is relatively uniform. SSH gradients in the SAZ are generally weak (Figs. 5 and 6) and the distribution of ∇SSH is not as sharply peaked about this core value as found for the ACC fronts (Fig. 4). The enhanced SSH gradients north of the SAF do not correspond to the STF, which has little signature in SSH (see above). Examination of hydrographic sections along 140°E suggests that the enhanced SSH gradients observed in the SAZ rather reflect perturbations in the depth of the pycnocline due to the presence of eddies and Rossby waves (not shown). The fact that Fig. 4 shows these gradient maxima cluster around a particular SSH value suggests that such features have a preferred propagation path (in SSH space).

### *e. Frequency distributions of the frontal pattern*

Having demonstrated that the fronts of the Southern Ocean can be traced reliably using SSH, we now use the weekly time series of SSH maps to characterize the variability of the ACC fronts in space and time. Variability in the path of the frontal jets is shown in Fig. 9, in the form of a two-dimensional histogram of the frequency of occurrence. The "meander envelopes" of each frontal branch are tight immediately upstream, over, or on the northern flank of topographic features. The envelopes are broader over the abyssal plains and downstream of topographic obstacles. On the whole, each front generally follows a single preferred path. However, in regions of complex bathymetry some of the frontal branches are characterized by a bimodal distribution. For example, the middle branch of the PF crosses the southern Macquarie Ridge (160°E) either through a trough at 57°S or farther south adjacent to the northern flank of the SEIR where it merges with the southern branch of the PF. The northern branch of the PF has a bimodal distribution near 140°E, where the front is deflected to the north by the SEIR.

### *f. Spatial variations in front intensity*

In Fig. 10, the SSH gradients are averaged over the 12 yr at each point along the frontal path and then normalized by the maximum gradient along each front (values used for the normalization are given in the caption of Fig. 10). The figure shows how the intensity of each front varies across the study region.

The SAF and PF branches are most intense just downstream of the crest of the SEIR. The SSH gradients associated with the SAF are also large south of the Campbell Plateau between 160° and 170°E. The SSH gradients are less intense where the flow is constrained by the bathymetry of the Macquarie Ridge at 160°E, which lies between these two maxima. The PF branches merge with the sACCf to form a region of enhanced gradients along the northern flank of the midocean ridge south of New Zealand. The weakest SSH gradients along the path of the PF are found where the fronts turn north as they encounter the shoaling topography of the SEIR. The sACCf and Bdy are most intense where they flow along the continental rise of Antarctica between 110° and 140°E. The SSH gradients along the SAZ feature are much stronger west of 140°E, where this contour is close to the SAF, than in the east where this contour is well north of the ACC. Overall, Fig. 10 illustrates that the intensity of the SSH gradients varies along the path of each front and the distribution is influenced strongly by bathymetry: the fronts are more intense in deep water downstream of topographic obstacles (e.g., the SEIR and Macquarie Ridge) and SSH gradients tend to be enhanced on the northern flank of zonal ridges or slopes.

### *g. Temporal variability of the Southern Ocean fronts*

Since the fronts in the Southern Ocean are well approximated by contours of SSH, the temporal variance of SSH is a good indicator of the variability of the fronts. The standard deviation of SSH is shown in Fig. 11. This map is similar to both the gradient field of mean SSH given in Fig. 6, as well as the mean SSH gradient distribution sampled along the fronts (Fig. 10), as might be expected: temporal variations in SSH are large in zones of enhanced SSH gradients. However, there are some exceptions: for example, the large spatial gradients in SSH found on the northern flank of the midocean ridge south of New Zealand are not matched by a maximum in the standard deviation of SSH, because the shoaling topography to the south tends to stabilize the flow and minimize meandering of the fronts. Likewise, the large SSH gradients associated with the SAF west of 140°E, where the SAF lies on the northern side of the SEIR and is stabilized by the topography, correspond to relatively small temporal variability in SSH. Farther east, the mean spatial gradients of SSH are large over the sloping topography between 140° and 150°E, where the standard deviation of SSH is relatively small, and the spatial gradients are weak between 140° and 150°E, where the standard deviation is large. In other words, the standard deviation of the SSH

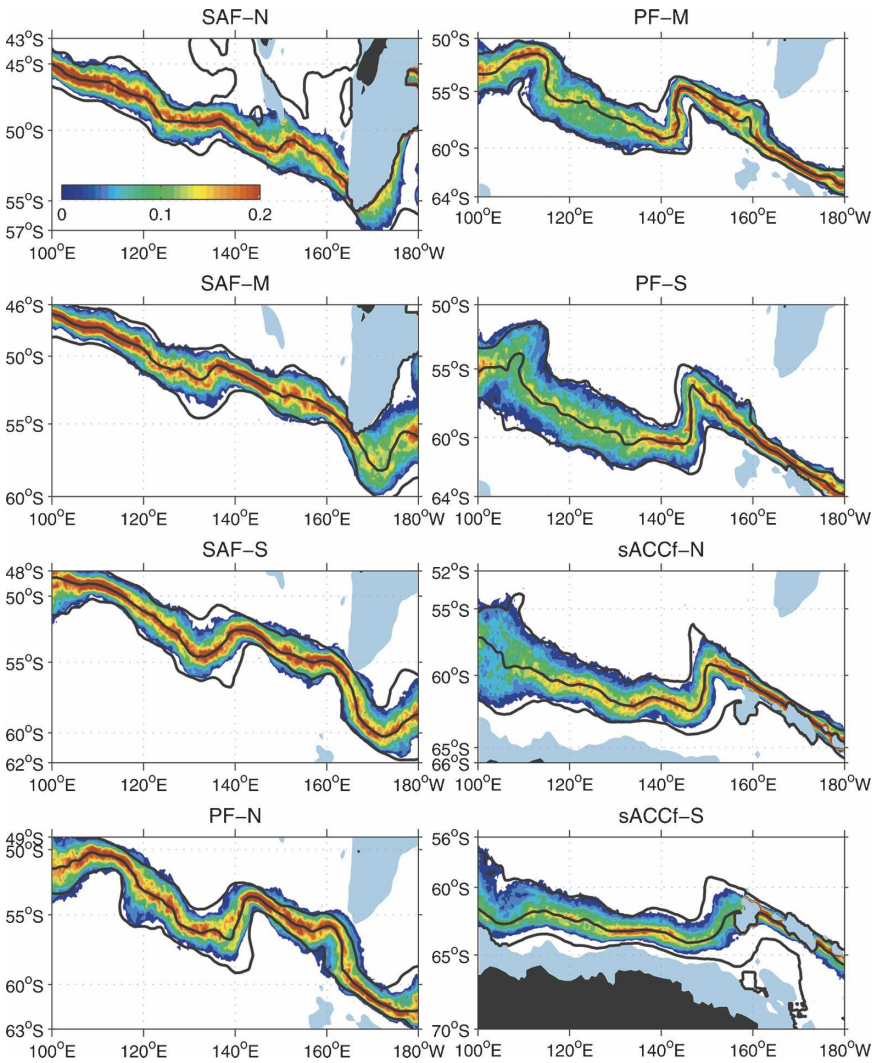


FIG. 9. The frequency of occurrence of the front positions at grid points where the fronts were observed at least in 6% of the time. Color range varies between 6% and 20%. The mean position of each frontal branch, derived by contouring the mean SSH field, is shown by the central thick solid line. Adjacent frontal branches are also shown by thick solid lines. Depths shallower than 2500 m are shaded.

map clearly illustrates the tendency for topography to either stabilize the flow (where the bottom slopes up to the south, reinforcing the planetary $\beta$ effect) or destabilize the flow (where the topography changes suddenly).

We can further characterize the nature of the variability of the Southern Ocean fronts by considering the distribution of the standard deviation of SSH in different period bands. Figures 12a–c show the contribution of mesoscale (periods less than 4 months), quasi-annual (4 months to 1.5 yr) variability, and interannual (periods more than 1.5 yr) variability to the total SSH variability at each location, respectively (plotted as a percentage of the total variance). The contribution of each time scale to the total variance shows different spatial patterns.

Mesoscale variability makes the dominant contribution (>50%) to the SSH variance south of the Campbell Plateau (where the total variance is high) and in the deep water of the Australian–Antarctic Basin between 110° and 140°E (where the total variance is relatively low). Both areas correspond to regions where eddy formation is common (eddies were identified by closed contours of SSH; not shown). The mesoscale band makes a modest contribution to the total variance along much of the path of the SAF and PF branches. The mesoscale contribution is small over the low point in the ridge at the Australian–Antarctic Discordance

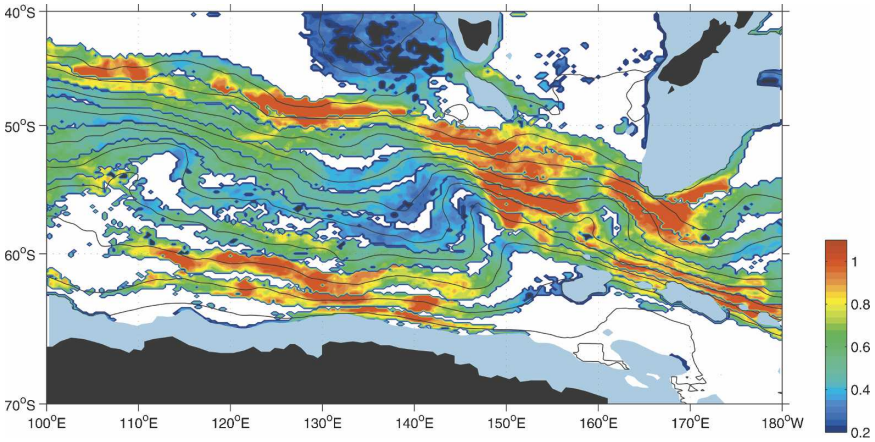


FIG. 10. Normalized SSH gradient distribution associated with the ACC frontal branches. Absolute SSH gradients for each front are normalized by the maximum gradient on that frontal branch to show how the front intensity varies across the study area. The maximum gradient values for each front are 0.126 m (100 km)$^{-1}$ (Bdy); 0.164 and 0.205 (southern and northern branches of sACCf); 0.271, and 0.357, 0.428 (PF); 0.521, 0.512, and 0.436 (SAF); and 0.287 (SAZ). Depths shallower than 2500 m are shaded.

(50°S, 120°–130°E) and where the fronts turn north over the western flank of the SEIR.

Quasi-annual variability makes the dominant contribution to the total variance in the SAZ, west of Tasmania (where SSH variability is weak). Quasi-annual variability accounts for more than 50% of the total variance over the western part of the Australian–Antarctic Basin, where the depth gradually increases downstream and the branches of the PF turn to the south.

Interannual variations dominate the total SSH variance in the SAZ between Tasmania and New Zealand, over the western flank of the SEIR where the fronts deflect to the north, and near the Australian–Antarctic Discordance (50°S, 120°–130°E; Fig. 11). The total variance is relatively small in these regions. The maximum in the relative contribution of interannual variability over the SEIR suggests that on these time scales the ACC may respond to changes in forcing by altering the flow path relative to the topography (rather than, e.g., changing the intensity of the flow). Examination of individual maps of SSH filtered in this period band suggest that the SSH anomalies reflect coherent shifts of the frontal branches over the western flank of the SEIR (e.g., to the north and west during periods of low SSH, and vice versa).

## 5. Discussion

As noted by Hughes and Ash (2001), there is a curious discrepancy between the traditional picture of the

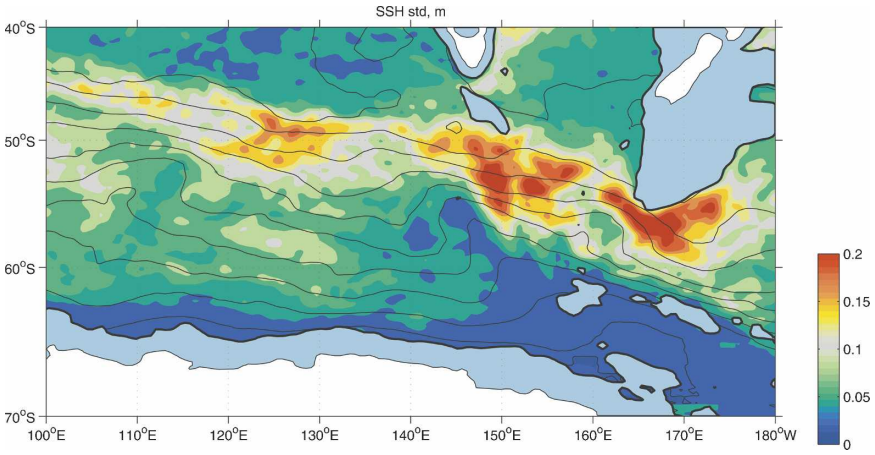


FIG. 11. Standard deviation of sea surface height (m).

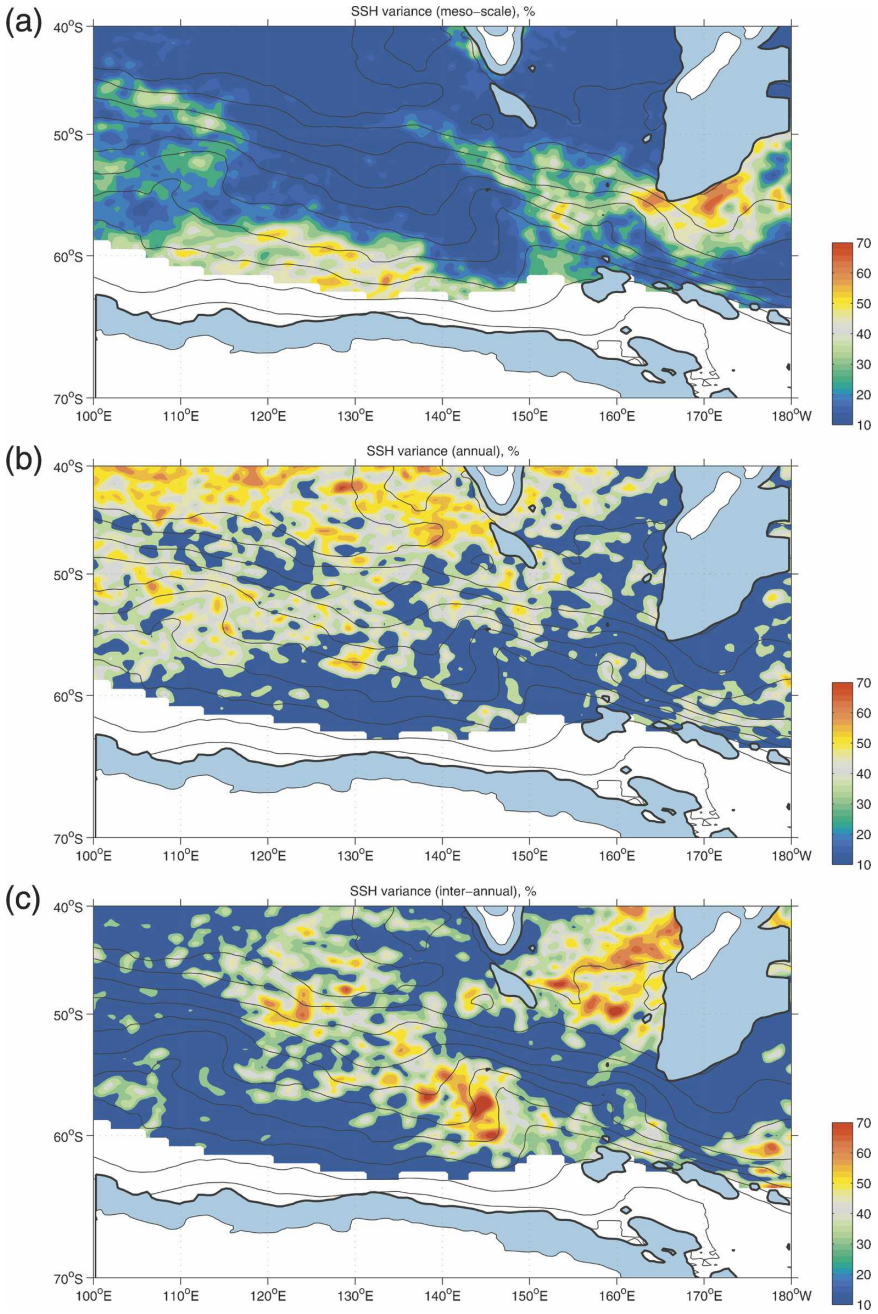


FIG. 12. Contribution of (a) mesoscale, (b) annual, and (c) interannual SSH variability to the total SSH variability (% of variance).

ACC jets developed from analysis of hydrographic sections and that derived from high-resolution numerical models and remote sensing. Hydrographers are able to trace three continuous circumpolar fronts, which correspond to particular water mass features along their entire path (e.g., Orsi et al. 1995; Belkin and Gordon 1996). The continuity and stability (in a water mass sense) of the fronts seems at odds with the convoluted web of filaments that is commonly observed in numerical simulations of sufficient resolution or in gradients of remotely sensed sea surface temperature or height (e.g., Maltrud et al. 1998; Best et al. 1999; Hughes and Ash 2001).

Our study suggests that the apparent discrepancy can be reconciled by recognizing the filamented but robust structure of the ACC. Maps of SSH and SST consis-

tently show numerous narrow bands of enhanced gradients (e.g., Fig. 1); the spatial and temporal persistence of these features is demonstrated by their appearance even in long-term mean gradient fields (e.g., Plate 1c in Hughes and Ash 2001). The complex and patchy distribution of $\nabla$SSH in synoptic maps gives the impression of a turbulent field, with little underlying structure. But we have shown that regions of enhanced $\nabla$SSH (i.e., fronts) are in fact aligned consistently with specific values of SSH. SSH contours approximate streamlines in an equivalent-barotropic flow like the ACC (Killworth and Hughes 2002), and streamlines also correspond to a particular water column structure in such a flow (Watts et al. 2001). For example, Watts et al. (2001) and Sun and Watts (2001) show that in the Southern Ocean the vertical profile of temperature and salinity can be accurately inferred from integral measurements such as sea surface height or acoustic travel time. This implies that front definition criteria based on water mass properties will also coincide with particular values of SSH.

We conclude that both points of view are valid: the ACC is made up of multiple filaments and each of those filaments corresponds to particular water mass features that are clearly related to one of the primary Southern Ocean fronts. Fronts split into multiple branches or merge to form "superfronts" and the intensity of the fronts varies along the circumpolar path. The splitting and merging of fronts has now been observed in numerous high-resolution hydrographic and expendable bathythermograph (XBT) sections [e.g., Nowlin et al. 1977; Read et al. 1995; Sparrow et al. 1996; Rintoul et al. 1997; SR02; Budillon and Rintoul 2003; multiple fronts are also evident in many Southern Ocean World Ocean Circulation Experiment (WOCE) sections; see plates in Orsi and Whitworth (2005)]. In past studies of single sections, some of these fronts may have been dismissed as transient or local features of limited interest.

Theory and high-resolution numerical modeling experiments suggest that multiple jets are a robust feature of the ACC (and other planetary flows) (e.g., Rhines 1975; Williams 1978; Panetta 1993). In flat-bottom channel models of sufficient meridional scale (wide relative to the first baroclinic Rossby radius), eddy–mean flow interactions create multiple jets. Interactions between flow and topography can also produce multiple jets (as well as altering the nature of the eddy–mean flow interaction) (e.g., Treguier and Panetta 1994; MacCready and Rhines 2001; Tansley and Marshall 2001). The new contribution of the present study is to show that the multijet structure of the ACC predicted by theory and seen in realistic numerical models is also observed, that the multiple jets are aligned consistently with particular streamlines, and that these streamlines are in turn coincident with particular water mass structures. We can therefore make the link between the filaments observed in remote sensing observations and the "classical" fronts identified in hydrographic data.

## 6. Conclusions

In conclusion, we find that the multiple jets of the ACC fronts are consistently aligned with particular streamlines (SSH contours). The association between the jets and streamlines is remarkably robust, surviving despite vigorous interactions between the mean flow, eddy field, and topography. The results help to bridge between the two disparate views of the ACC fronts derived from hydrographic data (continuous, circumpolar fronts defined by water mass features) and from theory, remote sensing, and high-resolution simulations (discontinuous filaments). The multiple jets of the ACC merge and diverge and change in intensity across the Australian sector, often as a result of interactions with topography, causing the patchiness observed in the $\nabla$SSH fields. But the alignment between the jets and streamlines (and hence water mass features) persists, and in this sense the ACC jets are continuous. The existence of multiple jets helps explain why previous studies have not agreed on the location of the Subantarctic and Polar Fronts: the different hydrographic criteria used in these studies picked out different branches of the primary fronts. Using SSH as a proxy for the fronts, we can characterize the structure and variability of the ACC fronts with much higher resolution than previously possible (a few weeks in time and 50–100 km in space). The SSH maps indicate that the path, width, and intensity of the fronts are influenced strongly by the bathymetry. The frontal branches tend to be distinct over abyssal plains and to merge on the northern slope of ridges or where diverted to the south by obstacles like the Campbell Plateau. The meander envelope of each front is narrower on the northern flank of ridges, where the topographic slope enhances the planetary $\beta$ effect, and broader over flat topography.

*Acknowledgments.* This work is supported by the Australian Greenhouse Office of the Department of Environment and Heritage, Australia, and the Cooperative Research Centre program of the Australian government. The research is a contribution to the CSIRO Wealth from Oceans National Research Flagship.

We are pleased to contribute this work as an addition to a series of papers (that appeared in the February

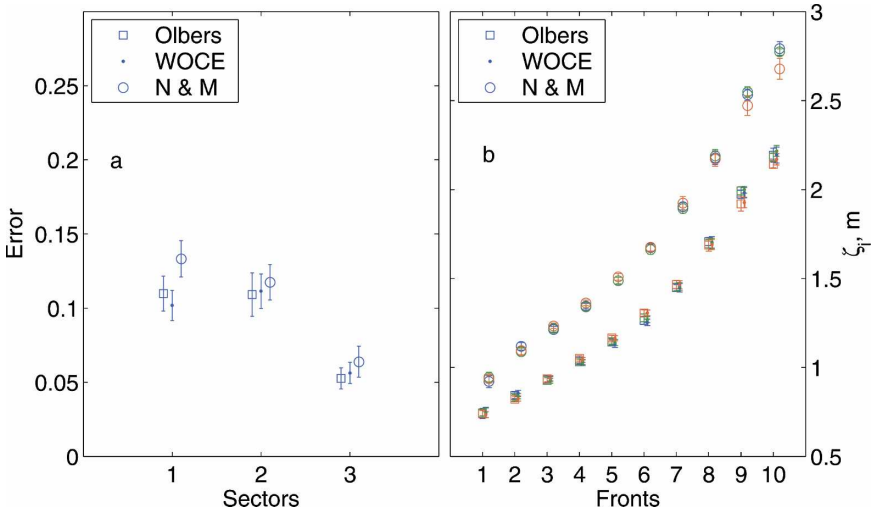


FIG. A1. Sensitivity of optimization to the dynamic height climatology: (a) mean optimization error, $n = 10$, in each sector (sector 1 = 100°–130°E; 2 = 130°–160°E; 3 = 160°–180°E) and (b) optimal contours $\zeta_i$, using Gouretski and Koltermann (2004), Olbers et al. (1992), and Niiler et al. (2003) climatologies. Symbols are offset on $x$ axis for clarity. In (b), blue, green, and red correspond to sectors 1, 2, and 3, respectively.

2007 *Journal of Physical Oceanography*) honoring the contribution Carl Wunsch continues to make to science. The hydrographic data and altimetry data used in this study were both collected by programs that Carl was instrumental in getting off the ground (TOPEX/Poseidon) or out to sea (the World Ocean Circulation Experiment). Carl has made an immense contribution to improving our understanding and observations of the low-frequency variability of the ocean, through his advocacy for new approaches to observing the ocean and the development of new tools for the rigorous analysis and interpretation of those observations. Carl's approach to science continues to inspire many of us who have worked with him.

## APPENDIX

### Sensitivity to the Dynamic Height Climatology

We carried out a similar analysis with two other dynamic height climatologies to test the sensitivity of the results to the mean field used. The WOCE global hydrographic climatology (Gouretski and Koltermann 2004), like the Olbers et al. (1992) climatology, is derived from hydrographic data. The WOCE product includes more recent data than the older Olbers climatology, but most of the stations used are common to both maps. The main difference between the two is in the choice of interpolation scales used to map the mean fields: the WOCE atlas is more highly smoothed than the older Olbers fields, as seen below. The third climatology used is entirely independent of hydrographic data. Niiler et al. (2003) derived a geostrophically balanced absolute sea level climatology from drifter velocity observations (measured winds were used to remove the Ekman drift and altimetry was used to correct for the temporal bias in the drifter observations). The authors note that their estimates of absolute sea level differences in the Southern Ocean appear to be overestimated, due to slippage of the drifters in the high wind and wave climate typical of the region. Despite the bias of the Niiler et al. climatology in the Southern Ocean, we include it in the sensitivity tests because it provides an independent climatology with high spatial resolution. The Niiler climatology represents the mean field over the period 1992–2002. The other climatologies are based on data covering the period between the 1960s and the present, but with very irregular sampling in time and space.

The main conclusion of the paper—that the jets of the ACC are consistently aligned with particular streamlines—holds for each of the climatologies used. In each case, fitting 10 SSH contours to the SSH gradient fields is sufficient to account for 85%–95% of the total area occupied by the SSH gradient extrema (Fig. A1a). For the two hydrography-based climatologies, nearly identical SSH values are found to correspond to each front, with similar (small) uncertainties (Fig. A1b). The Niiler climatology results in best-fit SSH values that are systematically higher by a factor of about 1.3, but otherwise show a similar pattern.

Figure A2 shows an example of a synoptic SSH gra-

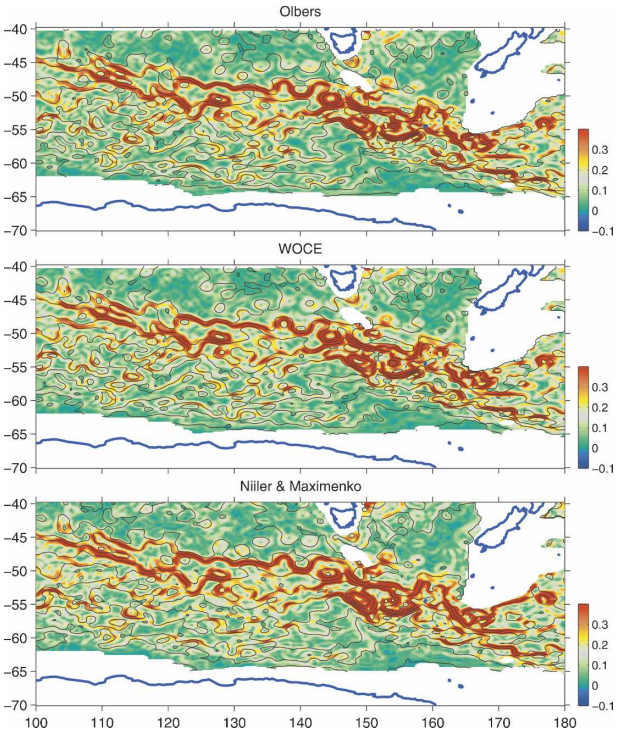


FIG. A2. Total SSH gradient (anomaly + mean field) on 11 Nov 1992 using three different mean fields (color). The optimal contours $\zeta_i$ (determined from the fits to the 12-yr sequence of SSH gradient maps) are overlaid on each map (black contours).

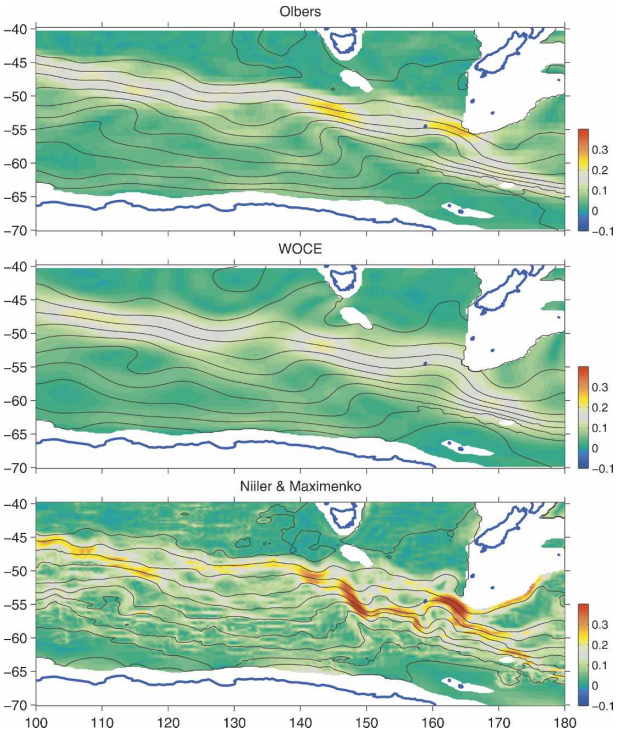


FIG. A3. Mean locations of the ACC fronts (i.e., the optimal contours $\zeta_i$) determined from the fits to the SSH gradient distribution for each climatology considered. SSH gradients of the mean fields are shown in color.

dient field using the three different climatologies, overlaid with the best-fit SSH contours optimized for the whole period of observations. The synoptic SSH gradient fields are very similar, demonstrating that the SSH anomalies dominate the synoptic $\nabla$SSH pattern. The gradient field associated with the mean dynamic height fields (Fig. A3) rarely exceeds the threshold used to identify the ACC fronts [$\nabla\zeta > 0.25$ m (100 km)$^{-1}$] and therefore has little influence on the inferred location of the fronts in the synoptic maps.

As a result, the location of the fronts in the synoptic maps is also very similar for the three climatologies, as can be seen in Fig. A2. To assess the difference in the front locations in a more quantitative way, we determine the distance $D_\zeta$ between optimized contours derived using the different climatologies $j$ and $k$ as

$$D_\zeta = 2S_\zeta/(\ell^j + \ell^k),$$

where $S_\zeta$ is the total area between the contours $\zeta_i^j$ and $\zeta_i^k$, and $\ell^j$ and $\ell^k$ are their respective lengths, for each frontal branch $i$ (see Fig. A4a for further explanation). As expected, the front positions derived using the two hydrography-based climatologies are most similar, with the mean distance between the optimal contours not exceeding 20 km (Fig. A4b). The difference is less than the estimated lateral extent of the frontal branches given in Fig. 3. Only the positions of the southernmost ACC front (Bdy, $i = 1$) and enhanced SSH gradients in the SAZ ($i = 10$) differ by more than 20 km, which is consistent with the larger optimization errors found for these regions. The distance between the fronts derived using the hydrography-based climatology and the Niiler climatology is greater (about 30 km), but still less than the width of the frontal branches. We conclude that the synoptic location of the ACC fronts inferred using SSH is insensitive to the choice of mean field, with differences smaller than the width of the front and much smaller than the meander envelope of each front, reflecting the fact that the anomalies of SSH dominate the $\nabla$SSH maps.

Nevertheless, the mean location of the best-fit contours does depend to some extent on the climatology used (as expected, since the mean of the SSH anomalies is small), as seen in Fig. A3. The SSH value corresponding to each best-fit contour also can depend on the climatology used. For the two hydrography-based climatologies, the inferred mean positions of the fronts are very similar, but not identical. The main difference is the greater smoothing in the WOCE maps (e.g., the

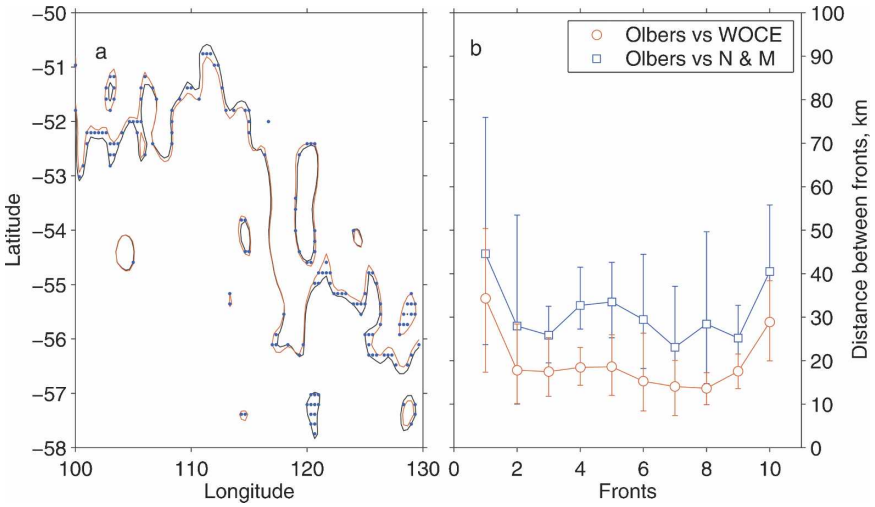


FIG. A4. Quantifying the difference between front positions inferred using different climatologies. (a) An example illustrating the method used. Red (black) lines are the position of northern PF inferred using the WOCE (Olbers) climatologies for a particular synoptic map. The area between the two fronts is indicated by blue dots. (b) Mean distance between the front positions, determined by dividing the area between the fronts by the average length of the contour (see text). Error bars are represented by 10th and 90th percentiles of the distance distributions.

"S-bend" of the fronts when passing over the SEIR near 145°E is smoothed out somewhat in the WOCE map). The Niiler et al. climatology is similar to the two hydrography-based climatologies on the large scale but shows more detailed spatial structure. Note that the Niiler et al. climatology is of absolute sea level, including the mean barotropic flow, while the other two mean fields include only the baroclinic flow. The averaging period and data distribution in each of the mean fields is also different in each case. The fact that the location of the fronts is insensitive to the choice of mean field suggests that the averaging period and presence or absence of the mean barotropic contribution to sea level do not introduce significant uncertainties in the frontal maps, particularly for synoptic mapping of the fronts.

## REFERENCES


Belkin, I. M., and A. L. Gordon, 1996: Southern Ocean fronts from the Greenwich Meridian to Tasmania. *J. Geophys. Res.,* **101,** 3675–3696.

Best, S. E., V. O. Ivchenko, K. J. Richards, R. D. Smith, and R. C. Malone, 1999: Eddies in numerical models of the Antarctic Circumpolar Current and their influence on the mean flow. *J. Phys. Oceanogr.,* **29,** 328–350.

Budillon, G., and S. R. Rintoul, 2003: Fronts and upper ocean thermal variability south of New Zealand. *Antarct. Sci.,* **15,** 141–152.

Deacon, G. E. R., 1937: The hydrology of the Southern Ocean. *Discov. Rep,* **15,** 1–124.

Ducet, N., P. Y. Le Traon, and G. Reverdin, 2000: Global high-resolution mapping of ocean circulation from TOPEX/Poseidon and *ERS-1* and *-2*. *J. Geophys. Res.,* **105** (C8), 19 477–19 498.

Gille, S. T., 1994: Mean sea-surface height of the Antarctic Circumpolar Current *Geosat* data: Method and application. *J. Geophys. Res.,* **99** (C9), 18 255–18 274.

Gordon, A. L., 1972: On the interaction of the Antarctic Circumpolar Current and the Macquarie Ridge. *Antarctic Oceanology II: The Australian-New Zealand Sector,* D. E. Hayes, Ed., Antarctic Research Series, Vol. 19, Amer. Geophys. Union, 71–78.

Gouretski, V. V., and K. P. Koltermann, 2004: WOCE global hydrographic climatology. Tech. Rep. 35, Berichte des BSH, 54 pp.

Hughes, C. W., and E. Ash, 2001: Eddy forcing of the mean flow in the Southern Ocean. *J. Geophys. Res.,* **106,** 2713–2722.

Killworth, P. D., and C. W. Hughes, 2002: The Antarctic Circumpolar Current as a free equivalent-barotropic jet. *J. Mar. Res.,* **60,** 19–45.

Le Traon, P., F. Nadal, and N. Ducet, 1998: An improved mapping method of multisatellite altimeter data. *J. Atmos. Oceanic Technol.,* **15,** 522–534.

MacCready, P., and P. B. Rhines, 2001: Meridional transport across a zonal channel: Topographic localization. *J. Phys. Oceanogr.,* **31,** 1427–1439.

Maltrud, M. E., R. D. Smith, A. J. Semtner, and R. C. Malone, 1998: Global eddy-resolving ocean simulations driven by 1985–1994 atmospheric winds. *J. Geophys. Res.,* **103,** 30 825–30 853.

Maximenko, N. A., B. Bang, and H. Sasaki, 2005: Observational evidence of alternating jets in the World Ocean. *Geophys. Res. Lett.,* **32,** L12607, doi:10.1029/2005GL022728.

McWilliams, J. C., W. R. Holland, and J. Chow, 1978: A description of numerical Antarctic Circumpolar Currents. *Dyn. Atmos. Oceans,* **2,** 213–291.

Moore, J., M. Abbott, and J. Richman, 1999: Location and dy-

namics of the Antarctic polar front from satellite sea surface temperature data. *J. Geophys. Res.,* **104,** 3059–3073.

Morrow, R., A. Brut, and A. Chaigneau, 2003: Seasonal and interannual variations of the upper ocean energetics between Tasmania and Antarctica. *Deep-Sea Res. I,* **50,** 339–356.

Munk, W. H., and E. Palmén, 1951: Note on the dynamics of the Antarctic Circumpolar Current. *Tellus,* **3,** 53–55.

Nakano, H., and H. Hasumi, 2005: A series of zonal jets embedded in the broad zonal flows in the Pacific obtained in eddy-permitting ocean general circulation models. *J. Phys. Oceanogr.,* **35,** 474–488.

Niiler, P. P., N. A. Maximenko, and J. C. McWilliams, 2003: Dynamically balanced absolute sea level of the global ocean derived from near-surface velocity observations. *Geophys. Res. Lett.,* **30,** 2164, doi:10.1029/2003GL018628.

Nowlin, W. D., Jr., and M. Clifford, 1982: The kinematic and thermohaline zonation of the Antarctic Circumpolar Current at Drake Passage. *J. Mar. Res.,* **40** (Suppl.), 481–507.

——, T. Whitworth, and R. D. Pillsbury, 1977: Structure and transport of Antarctic Circumpolar Current at Drake Passage from short-term measurements. *J. Phys. Oceanogr.,* **7,** 788–802.

Olbers, D., V. Gouretski, G. Seiß, and J. Schröter, 1992: *Hydrographic Atlas of the Southern Ocean.* Alfred Wegener Institute for Polar and Marine Research, 17 pp. + 82 plates.

——, D. Borowski, C. Völker, and J.-O. Wolff, 2004: The dynamical balance, transport and circulation of the Antarctic Circumpolar Current. *Antarct. Sci.,* **16,** 439–470.

Orsi, A. H., and T. W. Whitworth III, 2005: *Southern Ocean.* Vol. 1, *Hydrographic Atlas of the World Ocean Circulation Experiment (WOCE),* M. Sparrow, P. Chapman, and J. Gould, Eds., International WOCE Project Office, 223 pp.

——, ——, and W. D. Nowlin Jr., 1995: On the meridional extent and fronts of the Antarctic Circumpolar Current. *Deep-Sea Res. I,* **42,** 641–673.

Panetta, R. L., 1993: Zonal jets in wide baroclinically unstable regions: Persistence and scale selection. *J. Atmos. Sci.,* **50,** 2073–2106.

Peterson, R. G., and L. Stramma, 1991: Upper-level circulation in the South Atlantic Ocean. *Progress in Oceanography,* Vol. 26, Pergamon Press, 1–73.

Pollard, R. T., M. I. Lucas, and J. F. Read, 2002: Physical controls on biogeochemical zonation in the Southern Ocean. *Deep-Sea Res. II,* **49,** 3289–3305.

Read, J. F., R. T. Pollard, A. I. Morrison, and C. Symon, 1995: On the southerly extent of the Antarctic Circumpolar Current in the southeast Pacific. *Deep-Sea Res. II,* **42,** 933–954.

Rhines, P. B., 1975: Waves and turbulence on a $\beta$-plane. *J. Fluid Mech.,* **69,** 417–433.

——, 1977: The dynamics of unsteady currents: Marine modeling. *The Sea,* E. D. Goldberg et al., Eds., Ocean Engineering Science, Vol. 6, John Wiley and Sons, 189–318.

——, 1989: Deep planetary circulation over topography: Simple models of midocean flows. *J. Phys. Oceanogr.,* **19,** 1449–1470.

——, 1994: Jets. *Chaos,* **4,** 313–339.

Rintoul, S. R., and J. L. Bullister, 1999: A late winter hydrographic section from Tasmania to Antarctica. *Deep-Sea Res. I,* **46,** 1417–1454.

——, J.-R. Donguy, and D. H. Roemmich, 1997: Seasonal evolution of upper ocean thermal structure between Tasmania and Antarctica. *Deep-Sea Res. I,* **44,** 1185–1202.

——, C. Hughes, and D. Olbers, 2001: The Antarctic Circumpolar Current system. *Ocean Circulation and Climate,* G. Siedler, J. A. Church, and J. Gould, Eds., Academic Press, 271–302.

Sievers, H. A., and W. D. Nowlin Jr., 1984: The stratification and water masses at Drake Passage. *J. Geophys. Res.,* **89,** 10 489–10 514.

Sinha, B., and K. J. Richards, 1999: Jet structure and scaling in Southern Ocean models. *J. Phys. Oceanogr.,* **29,** 1143–1155.

Sokolov, S., and S. R. Rintoul, 2002: Structure of Southern Ocean fronts at 140°E. *J. Mar. Syst.,* **37,** 151–184.

Sparrow, M. D., K. J. Heywood, J. Brown, and D. P. Stevens, 1996: Current structure of the south Indian Ocean. *J. Geophys. Res.,* **101,** 6377–6392.

Stammer, D., C. Wunsch, and R. M. Ponte, 2000: De-aliasing of global high frequency barotropic motions in altimeter observations. *Geophys. Res. Lett.,* **27,** 1175–1178.

Sun, C., and D. R. Watts, 2001: A circumpolar gravest empirical mode for the Southern Ocean hydrography. *J. Geophys. Res.,* **106,** 2833–2856.

Tansley, C. E., and D. P. Marshall, 2001: On the dynamics of wind-driven circumpolar currents. *J. Phys. Oceanogr.,* **31,** 3258–3273.

Treguier, A. M., and J. C. McWilliams, 1990: Topographic influences on wind-driven, stratified flow in a $\beta$-plane channel: An idealized mode for the Antarctic Circumpolar Current. *J. Phys. Oceanogr.,* **20,** 321–343.

——, and R. L. Panetta, 1994: Multiple zonal jets in a quasigeostrophic model of the Antarctic Circumpolar Current. *J. Phys. Oceanogr.,* **24,** 2263–2277.

Watts, D. R., C. Sun, and S. R. Rintoul, 2001: A two-dimensional gravest empirical mode determined from hydrographic observations in the subantarctic front. *J. Phys. Oceanogr.,* **31,** 2186–2209.

Webb, D. J., and B. A. de Cuevas, 2003: The region of large sea surface height variability in the southeast Pacific Ocean. *J. Phys. Oceanogr.,* **33,** 1044–1056.

Williams, G. P., 1978: Planetary circulations: I. Barotropic representations of Jovian and terrestrial turbulence. *J. Atmos. Sci.,* **35,** 1399–1426.

Wolff, J.-O., E. Maier-Reimer, and D. J. Olbers, 1991: Wind-driven flow over topography in a zonal $\beta$-plane channel: A quasi-geostrophic model of the Antarctic Circumpolar Current. *J. Phys. Oceanogr.,* **21,** 236–264.